Key Points:
- Snow deposition volume was more than twice that of snow erosion after a storm, though erosion was more spatially uniform than deposition
- Net mass gain over the area was small despite large local changes in snow depth
- Snow distribution changes did not lead to significant changes in spatial statistics of the surface

Changes in snow distribution and surface topography following a snowstorm on Antarctic sea ice

Ernesto Trujillo[1,2], Katherine Leonard[1,2,3], Ted Maksym[4], and Michael Lehning[1,2]

[1]School of Architecture, Civil and Environmental Engineering, École Polytechnique Fédérale de Lausanne, Lausanne, Switzerland, [2]WSL Institute for Snow and Avalanche Research SLF, Davos, Switzerland, [3]Cooperative Institute for Research in Environmental Sciences, University of Colorado Boulder, Boulder, Colorado, USA, [4]Woods Hole Oceanographic Institution, Woods Hole, Massachusetts, USA

Abstract Snow distribution over sea ice is an important control on sea ice physical and biological processes. We combine measurements of the atmospheric boundary layer and blowing snow on an Antarctic sea ice floe with terrestrial laser scanning to characterize a typical storm and its influence on the spatial patterns of snow distribution at resolutions of 1–10 cm over an area of 100 m × 100 m. The pre-storm surface exhibits multidirectional elongated snow dunes formed behind aerodynamic obstacles. Newly deposited dunes are elongated parallel to the predominant wind direction during the storm. Snow erosion and deposition occur over 62% and 38% of the area, respectively. Snow deposition volume is more than twice that of erosion ($351 \, \text{m}^3$ versus $158 \, \text{m}^3$), resulting in a modest increase of 2 ± 1 cm in mean snow depth, indicating a small net mass gain despite large mass relocation. Despite significant local snow depth changes due to deposition and erosion, the statistical distributions of elevation and the two-dimensional correlation functions remain similar to those of the pre-storm surface. Pre-storm and post-storm surfaces also exhibit spectral power law relationships with little change in spectral exponents. These observations suggest that for sea ice floes with mature snow cover features under conditions similar to those observed in this study, spatial statistics and scaling properties of snow surface morphology may be relatively invariant. Such an observation, if confirmed for other ice types and conditions, may be a useful tool for model parameterizations of the subgrid variability of sea ice surfaces.

1. Introduction

Snow distribution over sea ice plays important roles in physical and biological processes. Snow has a higher albedo and a lower thermal conductivity than sea ice, with marked effects on the internal energy balance. In winter, the snow cover can limit the thermodynamic growth of the ice [e.g., *Maykut and Untersteiner*, 1971; *Ledley*, 1993; *Powell et al.*, 2005], especially in the Antarctic where deep snow accumulations and high ocean heat flux can lead to basal melting [e.g., *Jeffries et al.*, 1998; *Lewis et al.*, 2011]. In the Artic, the spatial distribution of snow has been shown to influence the evolution of melt ponds [*Petrich et al.*, 2012; *Polashenski et al.*, 2012], which in consequence affects the surface albedo [*Perovich et al.*, 1998, 2002]. Similarly, snow accumulation can lead to isostatic adjustment allowing flooding of sea ice surfaces with ocean water, which enhances the formation of snow ice [e.g., *Eicken et al.*, 1995; *Jeffries et al.*, 1998; *Maksym and Markus*, 2008]. Snow limits light transmission, with effects on sea ice biological communities [e.g., *Soohoo et al.*, 1987; *Ackley and Sullivan*, 1994; *Fritsen et al.*, 1994; *Haas et al.*, 2001; *Raymond et al.*, 2009]. Snow distribution also affects the morphology of the surface, which strongly controls momentum transfer between surface winds and the ice [*Andreas and Claffey*, 1995], controlling sea ice displacement and deformation [*Guest and Davidson*, 1991]. Further, knowledge of the amount of accumulation on sea ice is also important for estimation of sea ice thickness from satellite altimeters in both hemispheres [*Kwok et al.*, 2006; *Maksym and Markus*, 2008; *Kurtz and Markus*, 2012].

Accumulation and distribution of snow on sea ice is largely controlled by the interactions between the different elements of the ocean-sea ice-snow-atmosphere system. Snowfall and winds interact with the sea ice and ocean surfaces, determining how much snow is accumulated, redistributed, sublimated, and transported to the surrounding open water [*Dery and Tremblay*, 2004]. Difficulties associated with quantifying these mass (and energy) fluxes have limited our understanding of each of the processes involved. For example, snowfall

events are often accompanied by strong winds, and direct measurement of snowfall amounts and separation of snowfall as opposed to blowing snow have proven to be difficult. At larger scales, estimation of snowfall amounts on sea ice have been inferred from atmospheric reanalysis products [e.g., *Bromwich et al.*, 1995; *Maksym and Markus*, 2008], which have not been directly validated over sea ice. Such estimations also fail to account for the amount of blowing and drifting snow that is actually lost to open water between ice floes (leads), which can amount to a significant portion of the total yearly mass balance [*Eicken et al.*, 1994; *Leonard and Maksym*, 2011]. *Eicken et al.* [1994] estimated that as much as 100 mm yr^{-1} was lost to leads from data from the Weddell Sea; however, there are scarce observations to better address this question over larger scales. Similarly, *Dery and Tremblay* [2004] estimated that as much as 30% of annual snowfall was lost through sublimation of blowing snow, based on their observations during the Surface Heat Budget of the Arctic Ocean (SHEBA) experiment. Ultimately, blowing and drifting snow can severely inhibit snow accumulation, significantly affecting the surface mass balance of sea ice.

Wind transport of snow is ubiquitous over sea ice. Threshold wind speeds (at 10 m height) for entrainment of snow particles can range between 4 and 19 m s^{-1} conditioned to snow characteristics and environmental conditions both in the field [*Li and Pomeroy*, 1997] and in wind tunnel experiments [*Clifton et al.*, 2006]. Such wind speeds are commonly exceeded over sea ice [*Andreas and Claffey*, 1995], leading to variability in snow depth on an individual floe comparable to, or greater than, the observed regional variability in snow depth [*Sturm et al.*, 1998]. At the same time, ridges and ice blocks serve as aerodynamic obstacles that modify wind transport over the surface and enhance deposition of drifting and blowing snow. Resultant dunes and drifts may extend for tens of meters across the ice floe, causing high spatial variability in snow depth over short spatial scales [*Massom et al.*, 2001; *Filhol and Sturm*, 2015]. Snow transport processes modify the surface topography and hence affect the geometric roughness of sea ice, resulting in changes in the aerodynamic roughness of the surface [*Sturm et al.*, 1998; *Andreas and Claffey*, 1995]. Good characterization of aerodynamic roughness is necessary for accurate representation of sea ice-atmosphere interactions and sea ice dynamics in larger scale models. Accurate, detailed and spatially representative measurements of the topographic changes caused by snow redistribution have been difficult to obtain with traditional surveying methods. Also, surveying these changes requires careful timing relative to snow transport events, which can be challenging in the extreme conditions generally present in polar environments.

The evolution of sand bedforms due to aeolian transport has been extensively studied [e.g., *Cornish*, 1914; *Bagnold*, 1941; *Livingstone et al.*, 2007]. Similarities between snow and sand bedforms have long been recognized [*Cornish,* 1914], but received considerably less attention. The variety of snow dunes and bedforms observed, and mechanisms for genesis, have recently been reviewed by *Filhol and Sturm* [2015]. On sea ice depositional forms typically take the form of crescent-shaped barchans or whaleback dunes [e.g., *Sturm and Massom*, 2009]. Barchan dunes commonly form on relatively level ice [*Massom et al.*, 2001; *Petrich et al.*, 2012]. Because of the ubiquitous presence of ice blocks in ridge sails and rubble that form aerodynamic obstacles, snowdrifts are very common on sea ice. These form in the lee of these obstacles and can extend for up to tens of meters from the obstacle [*Radionov et al.*, 1997; *Sturm et al.*, 1998, 2002; *Massom et al.*, 2001]. Due to changing wind directions relative to the floe orientation, drift deposits typically form aprons on both sides of the ridge so that deeper snow is often associated with ridges [*Tin and Jeffries,* 2001; *Sturm et al.*, 2002], and more heavily deformed floes may tend to support deeper snow cover. This relative wind rotation also leads to cross bedding of snow dunes on level ice [*Sturm and Massom*, 2009]. Aeolian erosion of drifts and dunes sculpts the drifts and dunes into sastrugi [e.g., *Leonard*, 2009]. Although drifts, dunes, and sastrugi have different processes of formation, for simplicity in this study we refer to all aeolian snow structures as dunes.

Despite decades of observations of snow depth distribution [e.g., *Worby et al.*, 1996; *Ozsoy-Cicek et al.*, 2013], the spatial statistical properties of snow structures on sea ice have received comparatively little attention. In the Arctic, *Radionov et al.* [1997] developed a relationship between ridge heights and adjacent snow depths. *Sturm et al.* [2002] showed that the characteristic snow structure size at the SHEBA drift camp was about 20 m, and relatively independent of ice type, though *Petrich et al.* [2012] found more variability on fast ice near Barrow, Alaska. In the Antarctic, *Sturm et al.* [1998] reported snow structure lengths varying from 3 to 70 m, with means of 13–23 m. At both poles, the ice structure length was less than that for snow—thus, snow deposition plays an important role in modulating the surface roughness of the ice. Most of these studies have relied on point measurements along one-dimensional transects, and very few studies provide detailed

information on the local temporal evolution of the snow depth distribution as a result of precipitation and blowing snow events.

Capturing the impact of a snowstorm with blowing snow on sea ice is challenging. To do so, one must capture the local patterns of deposition and erosion, which as evidenced by observations of snow surface topography will have impacts on a range of spatial scales [e.g., *Massom et al.*, 2001], yet a single event may have a fairly minor impact on mean snow depth [*Sturm et al.*, 2002]. It is also desirable to capture this level of detail on scales greater than the largest snow depth features (i.e., of order 50 m) so that estimates of the aggregate impact can be robustly made. This requires repeat high-resolution spatial mapping. One method used for snow depth mapping in terrestrial environments over the last decade involves terrestrial laser scanning (TLS), which permits highly detailed (submeter) and spatially distributed surveying of surface topography [e.g., *Prokop*, 2008; *Prokop et al.*, 2008; *Grünewald et al.*, 2010; *Schirmer et al.*, 2011]. In these studies, repeated scans of the snow surface allow the determination of both snow depth and snow depth changes at high resolutions over significant spatial scales. *Polashenski et al.* [2012] carried out the only similar study (i.e., with repeat surveys) on sea ice to monitor melt pond formation and drainage. This study is notable as they were able to achieve precision repeat surveys with centimeter-level accuracy.

Herein, we present the first repeated measurements of snow surface topography before and after a storm and blowing snow event on Antarctic sea ice at very high spatial (~10 cm) and vertical resolution (~1 cm) using TLS over an area of 100 m × 100 m. These measurements were accompanied by coincident observations of boundary layer meteorology and blowing snow to analyze the characteristics of the surface atmosphere during the snowstorm and its effects on the snow distribution and surface morphology of an Antarctic ice floe. As part of this analysis, we characterize the spatial structure of the surface topography in a pre-snow and post-snow/wind storm scenario at unprecedented resolution. The article is organized to first establish a reference framework of atmospheric and wind conditions from which the changes in the surface originated. Second, the consequences of the storm on the snow distribution, surface topography, and snow depth changes are analyzed. Lastly, potential implications of the observed changes relevant to subgrid representation in larger-scale models are addressed, together with possible implications for atmospheric drag parameterizations and sea ice mass balance.

2. Data and Methods

Detailed observations of surface meteorological parameters and snow surface topography were made during the Sea Ice Physics and Ecosystem eXperiment 2 (SIPEX-2) research voyage to East Antarctica in September–November 2012 [*Meiners et al.*, 2016]. Data collection during the experiment was performed over several sea ice floes along the voyage track (ice stations). The ice in this near-coastal area was generally heavily deformed, thick first year drifting pack ice [*Williams et al.*, 2015] with a deep snow cover [*Toyota et al.*, 2016]. This study focuses on observations of a snowstorm event during one ice station sampled between 20 October 2012 and 23 October 2012 (Figure 1; 65°16′S, 119°00′E upon arrival at the ice station). This floe was very heavily deformed, very thick ice with a mean thickness of 4.87 m [*Hutchings et al.*, 2015]) and many blocky ice features and ridges apparent on the surface (Figure 1). The spatial arrangement of ridges suggests the floe was an amalgam of smaller pan-shaped floes that had frozen together, with ridges at their boundaries. The snow was very deep (mean of 52 cm—measured over the floe at ~2–3 m spatial resolution with an automated snow probe) with long, cross-hatched snow surface features (Figure 1). The thickness and ice core structure [*Hutchings et al.*, 2015] suggest this floe may have been multiyear ice, although other floes in the area were thick first year ice [*Williams et al.*, 2015], with similar snow depths [*Toyota et al.*, 2016] and surface topographic features.

Wind and snow transport information was collected using two wind masts temporarily placed on the ice floe, with Mast A recording for a period of 32 h between 20 October 2012 and 21 October 2012 and Mast B recording between 20 October 2012 and 23 October 2012 for a total of 81 h. Each of the wind masts consisted of three RM Young Wind Sentry anemometers (without vane) and one RM Young Wind Sentry vane and anemometer set on top of each mast (in total: wind speed at four heights and wind direction at one height), four Wenglor YH03NCT8 photoelectric sensors (snow particle counters) at four heights, and two laboratory calibrated Rotronics HC2-S3 temperature sensors with standard polyethylene filters. Wind speed and directions were averaged and total snow particle counts (particle radius > 100 μm [*Leonard et al.*, 2011]) were logged at
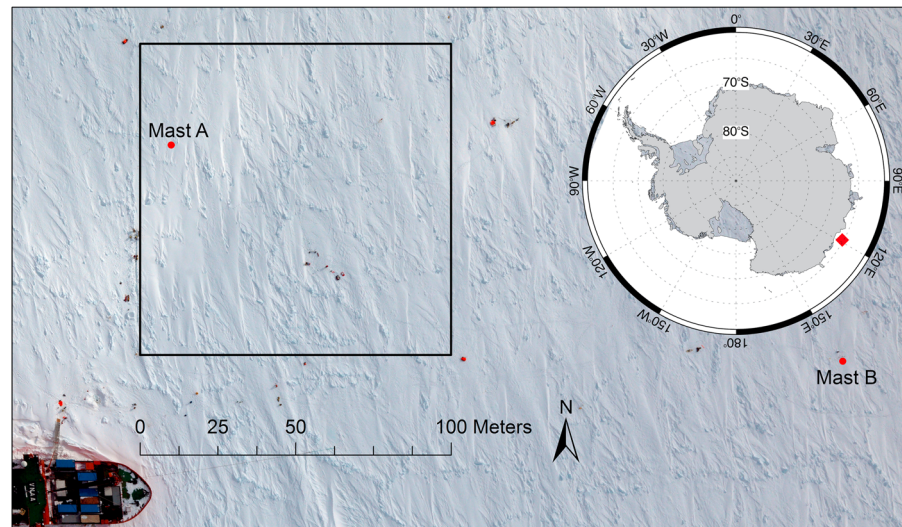
Figure 1. Location of the ice floe during the SIPEX-2 research voyage (red diamond marker) and layout of the instrumentation and surface plot. The black square delineates the study plot, while the red dots mark the location of the wind masts. The artificial north is aligned with the vertical boundary of the study plot. Image courtesy of Adam Steer and Jan Lieser of the Australian Antarctic Division (AAD) and the University of Tasmania.

10 s intervals. At Mast A, wind speed sensor heights were 0.60 m, 1.25 m, 1.96 m, and 2.58 m; wind direction at 2.58 m; Wenglor snow particle counters at 0.09 m, 0.44 m, 0.76 m, and 1.79 m; and temperature at 0.60 m and 1.93 m. At Mast B, wind speed sensor heights were 0.57 m, 1.10 m, 1.80 m, and 2.36 m; wind direction at 2.36 m; Wenglor snow particle counters at 0.04 m, 0.4 m, 0.6 m, and 1.66 m; and temperature at 0.52 m and 1.79 m (summarized in Table 1).

Surface topographic information was obtained using a terrestrial laser scanner (TLS, Leica C5). The operation requires the laser scanner to be positioned at several locations to eliminate scan shade behind ridges and other surface features, resulting in an integrated 3-D model of tens of millions of point returns for areas of tens to hundreds of meters. At this station, pre-storm and post-storm laser scans were achieved over the same 100 m × 100 m area. Each of these surveys was carried out during 7–8 h for 5–6 scan locations and in periods with no significant snow transport. Registration of the scans into a common coordinate system is the first step following acquisition. Individual errors for the targets/reflectors (eight in total), as determined by range differences between individual scans, are negligible, ranging between 0.1 cm and 0.9 cm, with a mean error of 0.4 cm for the 20 October 2012 surface and between 0.2 cm and 2.2 cm, with a mean error of 0.7 cm for the 23 October 2012 surface. After registration, point returns from occasional snow crystals and particles in the air were eliminated above the surface using several automated processing software routines that classify points by their location and relationships to the surface. See the accompanying dataset metadata for details [*Trujillo et al.*, 2016]. The resulting three-dimensional surfaces contain over 86 million points (average density = 8600+ points per m^2) for the pre-storm surface (date: 20 October 2012) and over 63 million points (6300+ points per m^2) for the post-storm surface (date: 23 October 2012). These final point clouds were then aggregated at grid scales between 1 cm to 1 m, with elevations relative to sea level. This binning process

Table 1. Instrument Heights Above the Snow Surface (in Meters) at the Two Mast Locations[a]

	Temperature			Wind Speed				Snow Particle Counters			
	L	U	Wind Direction	L	LM	UM	U	L	LM	UM	U
Mast A	0.60	1.93	2.58	0.60	1.25	1.96	2.58	0.09	0.44	0.76	1.79
Mast B	0.52	1.79	2.36	0.57	1.10	1.80	2.36	0.04	0.40	0.60	1.66

[a]Lower (L), lower middle (LM), upper middle (UM), and upper (U) mark the sensor location within each mast. Heights at Mast B remained unchanged after the storm.
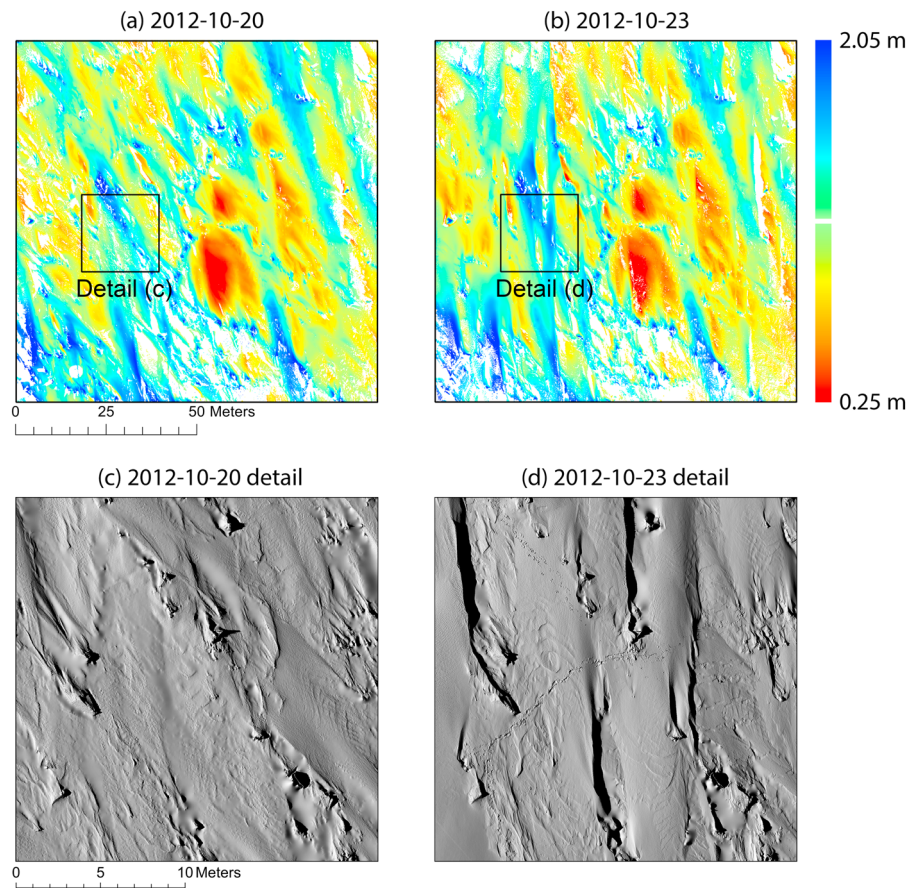
Figure 2. Surface elevations above sea level (10 cm horizontal resolution) over the 100 m × 100 m surface for the (a) pre-storm and (b) post-storm conditions. (c, d) Details revealed by the interpolated 1 cm surfaces for the pre-storm and post-storm conditions. The black squares in Figures 2a and 2b mark the location of the areas in Figures 2c and 2d.

helps reduce laser range precision errors/noise through averaging. Additionally, the 1 cm product was used to produce an interpolated surface to fill in the gaps in the surface. The 10 cm surfaces cover 81% and 79% of the 100 m × 100 m area for the pre-storm and post-storm surfaces, respectively. When overlapped to determine elevation change, the intersection of the two 10 cm surfaces covers 70% of the 100 m × 100 m area (Figures 2a and 2b). The remaining 30% of the area is those 10 cm bins that do not have a laser range for both scans. When binning at 1 m, the gap areas are reduced to 1.1% and 1.5% for each survey, respectively, and 2.3% for the elevation change map. The higher-resolution data are more useful for examining changes in surface structure, while the 1 m map is useful for estimating area-averaged statistics. The 1 cm interpolated surface reveals substantial detail, such as small-scale (~30–50 cm) dune-like surface patterns, human footsteps, and penguin footprints (Figures 2c, 2d, and S1–S5 in the supporting information). The TLS data set described here is being published alongside the publication of this article [*Trujillo et al.*, 2016].

2.1. TLS Error Estimation

While registration errors as described above were negligible, there could be larger errors in the horizontal and vertical positions of individual points within the scan, which could translate into significant errors in calculated snow elevation changes. The Leica C5 has a stated position accuracy of 6 mm, and range accuracy of 4 mm, with a 2 mm precision in the modeled surface. Determining the errors in the elevation difference between two surveys is more challenging, since the size of these errors may vary depending on the particular environmental conditions during the surveys. However, we can estimate the error from the surveys themselves by comparing points known not to change in position.

Any change in position of the reflectors/targets used to coregister the different laser scans between the two surveys provides a measure of the error in the observed elevation difference. These targets are located just

outside of the outline of the squared area (Figure 1). This displacement was < 5.6 cm (<5.4 cm in the horizontal and < 1.3 cm in the vertical (z direction)) at all but one reflector/target, which was displaced by 16 cm. This larger error is likely due to a small shift in the position of that target. This provides a reasonable estimate of the range error (<6 cm), which for this geometry is effectively the horizontal error. This error is smaller than the bin sizes used.

The vertical error is more critical, since the observed elevation differences are relatively small. From the repeat scans of the fixed targets, the apparent vertical error is less than 1.3 cm. But we can also estimate this error from the data themselves. On average, the highest exposed ice block peaks visible in both scans are unlikely to have much or any snow deposition or erosion (also see Figure 6, where the two scans closely coincide at ridge peaks). We have analyzed the difference between scans for only those points (~3000) that compose such ice blocks (both using a minimum height cutoff above the tallest dunes and by detection of local maxima in the survey). The mean elevation change between surveys for these blocks was −1 cm, with a narrow distribution (standard deviation of 3 cm; RMSE of 2 cm). Note that this result is independent of bin size. This suggests that the error in the mean elevation change is ~1 cm and for individual bins ~ 3 cm. Thus, we are confident that the erosional and depositional features are accurately captured at the 10 cm bin scale.

In the following sections general statistical properties (probability distributions, moments, and correlations) of the pre-storm and post-storm surfaces are analyzed. These statistical properties at such high resolutions and over the spatial coverage in this study are useful for subgrid representations of surface processes in sea ice and atmospheric models, and are in themselves novel given the spatial resolution of the data set. Statistical distributions of the surface and two-dimensional correlation functions are used to describe whether the observed change in the surface topography reflect a change in general properties of the surface and on the spatial organization of the surface over the 100 m × 100 m extent.

Complementing these more traditional statistics, we use power spectral techniques to characterize the spatial structure of the ice floe surface. Spectral techniques have been used in the study of highly variable processes to determine scaling ranges, spectral slopes, fractal dimensions, and Haussdorf exponents. In the present context of snow surface analysis, the power spectrum properties (e.g., scale breaks and spectral slopes) are used to quantify characteristic scales of surface features and the degree of variability and roughness within scaling ranges, illustrated in section 3.2 below [e.g., *Trujillo et al.*, 2007, 2009]. For the power spectrum analysis, one-dimensional power spectral densities were obtained for each of the west to east (x) rows and each of the north to south (y) columns of the fields and then averaged over each direction. The methodology followed for the spectral analysis is described in detail in *Trujillo et al.* [2007].

3. Results

3.1. Winds and Drifting Snow

The wind mast data are analyzed for two periods. The first period represents the conditions prior to the snowstorm between the early hours of 20 October and the afternoon of 21 October (Figure 3). This period also corresponds to the period with overlapping records between the masts allowing us to establish the correspondence between the atmospheric conditions at the surface at two different locations on the ice floe. The second period represents the conditions during the snowstorm between 21 October 2012 and 23 October 2012 (Figure 4). Incoming shortwave from a separate radiometer mast (Figure 1) is included as reference for local sunrise and sunset times, together with sunrise and sunset times from http://www.esrl.noaa.gov/gmd/grad/solcalc/ for independent support (grey areas in Figures 3 and 4). On-ice shortwave radiation measurements were not collected during the snowstorm period because the mast had to be removed due to safety concerns.

3.1.1. Pre-storm Conditions

Temperatures, wind directions, and wind speeds at both mast locations show marked correspondence during the pre-storm period despite the separation of 228 m between the two masts (Figure 3). Note that wind directions are presented relative the ice floe so that rotations of the floe relative to the wind have been removed from the data. Linear regression r^2 values between the measured variables range between 0.67 and 1 for the 10 s time series and between 0.77 and 1 for the 1 min series (Table 2; p-values < 0.01; three sample scatter plots in Figure 3c). Temperature shows the highest correlations (~1), followed by wind direction
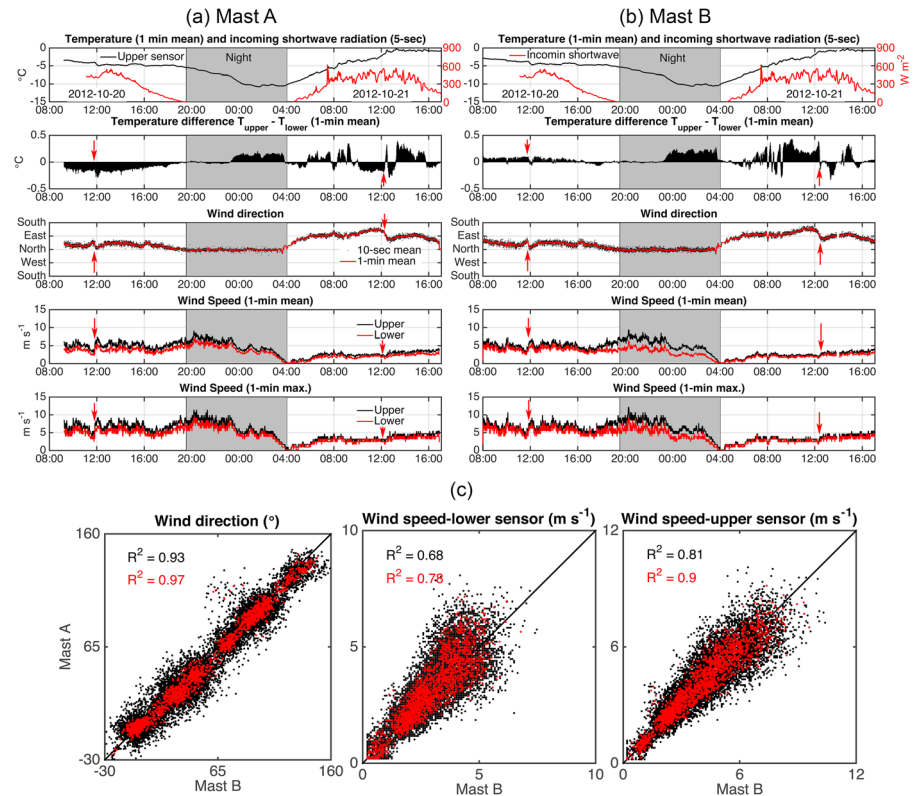
Figure 3. Surface air temperatures, wind speed, and direction at (a) Mast A and (b) Mast B for the pre-storm period. Wind directions are referenced to the fixed floe-centered artificial north indicated in Figure 1. Observed incoming shortwave radiation (red line, Figures 3a and 3b) indicates sunset and sunrise times (also delineated by the grey area, determined from http://www.esrl.noaa.gov/gmd/grad/solcalc/). Only wind speeds at the lower and upper sensors are shown for clarity. Red arrows highlight coincident features in the time series. (c) Comparison of wind speed and direction at the two masts, with black markers for the 10 s series and red markers for the 1 min series. r^2 values are obtained for linear regressions between the two variables.

(0.93 at 10 s and 0.97 at 1 min), and finally, wind speed (0.67–0.81 at 10 s and 0.77–0.90 at 1 min) and maximum wind speed (0.66–0.8 at 10 sec and 0.78–0.90 at 1 min).

Temperatures during the pre-storm period range between −11°C in the early hours of 21 October (~04:00, local time) and just below freezing (−0.1°C to −0.2°C) in the afternoon of 21 October (~16:00). Temperature differences between the upper and lower sensors provide a measure of atmospheric stability. While temperature differences (T_{diff}) between the two sensors are low at both masts ($|T_{diff}| < 0.2$°C) relative to the sensor absolute accuracy (estimated at ±0.1°C on average based on individual laboratory calibrations of the sensors), it is expected that the relative accuracy would be consistently much better over the short time period. To adjust for any potential calibration errors, temperature differences during the 20 highest wind speeds (upper anemometer) were averaged and then readjusted such that the average difference during this period of high speeds is set to zero. This adjustment is based on the argument that during the storm periods with drifting and blowing snow as well as overcast skies, the development of vertical temperature stratification is severely inhibited. This correction procedure was applied to the data from both masts. Once corrected, these data contain useful information regarding the evolution of the surface atmospheric conditions and the day-night and night-day transitions, as evidenced by the time series in Figures 3 and 4. Although the magnitude and sign of the readjusted temperature difference at the two heights (Figure 3a, second panel from top) is not always consistent between the two locations, similar behavior of the time series is clear. During this time there is an apparent increase in atmospheric stability during the night that is preserved until sunrise. During the daylight hours of 21 October, the temperature difference fluctuates rapidly, possibly due to variable shortwave heating and wind ventilation of the sensor during the light winds. There is often close correspondence between changes in the temperature difference and winds (vertical red lines in Figures 3a and 3b), possibly
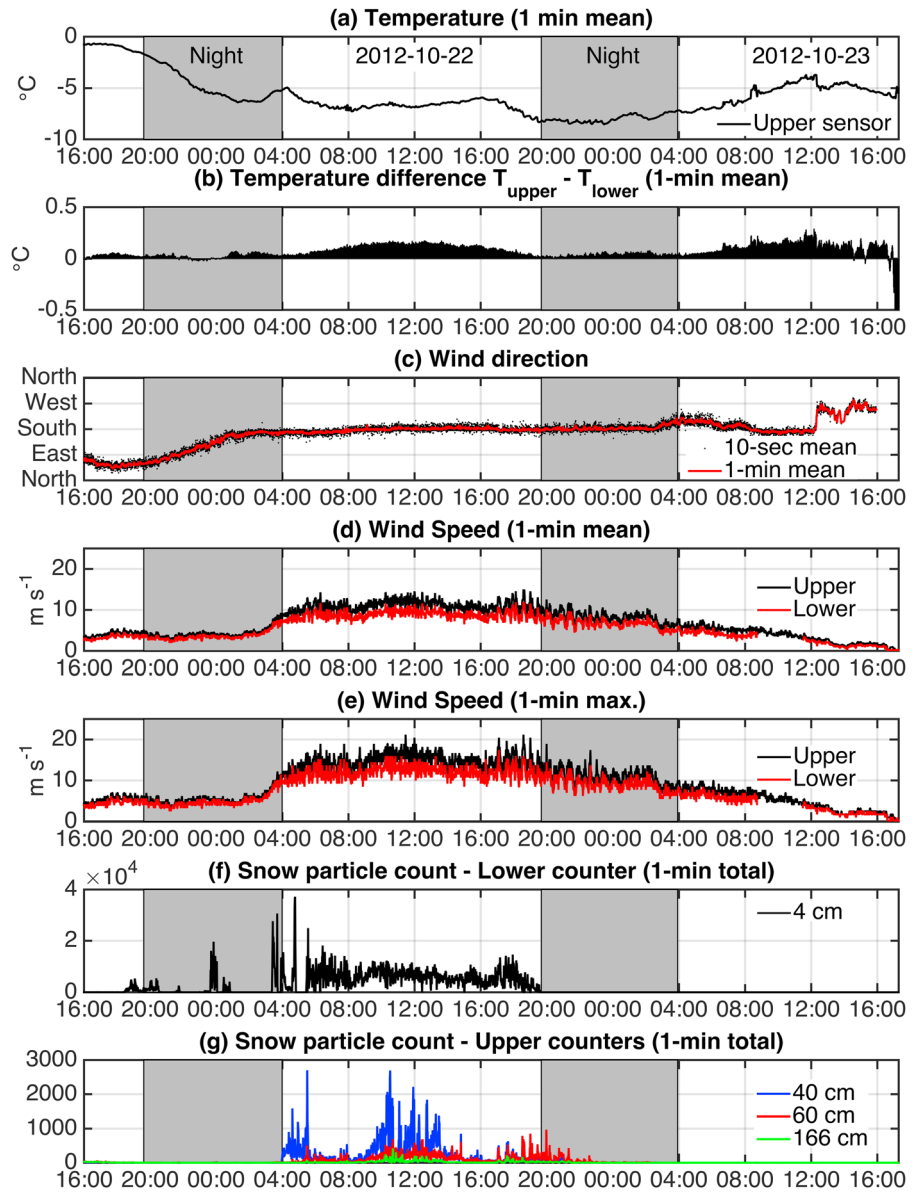
Figure 4. Surface air temperatures, temperature difference between upper and lower sensors, wind speed and direction, and blowing snow particle counts at Mast B for the storm period. Wind directions are referenced to the fixed floe-centered artificial north indicated in Figure 1. Sunset and sunrise times obtained from http://www.esrl.noaa.gov/gmd/grad/solcalc/ are used to delineate night periods. Only wind speeds at the lower and upper sensors are shown for clarity. (f and g) Snow particle counts are shown, separating the lowest counter from the upper counters (note the difference between the y axis scales).

Table 2. The r^2 Values Between Atmospheric Boundary Layer Parameters Measured at the Two Mast Locations[a]

	Temperature		Wind Direction	Wind Speed				Maximum Wind Speed			
	L	U		L	LM	UM	U	L	LM	UM	U
10 s	1	1	0.93	0.68	0.70	0.67	0.81	0.67	0.68	0.66	0.80
1 min	1	1	0.97	0.78	0.80	0.77	0.90	0.80	0.82	0.78	0.90

[a]The values correspond to 10 s and 1 min time intervals. Lower (L), lower middle (LM), upper middle (UM), and upper (U) mark the sensor location in each mast (see Table 1 for corresponding heights).

indicating advection of different air masses with different vertical temperature gradients. Wind speeds remained relatively low during the pre-storm period and presumably below the saltation threshold as no significant drifting snow was detected at this time. Comparison between winds at the two locations (Figure 3c) shows consistent wind speeds and direction so that wind conditions are consistent across the study area. Differences in wind speeds at the two locations increase as the speeds increase at both heights. This effect is more pronounced closer to the ice floe surface (confirmed by all four anemometers) demonstrating the disturbance to the wind flow caused by the surface features.

3.1.2. Storm Conditions

The transition to the snowstorm occurs during the evening of 21 October (Figure 4), with temperatures dropping below $-5°C$ and remaining between -5 and $-10°C$ throughout the storm. The vertical temperature difference varies little during the storm, with only a minor increase during the daylight hours and without exhibiting the high to low fluctuations present prior to the storm on 21 October. The transition to the storm conditions also includes a rotation of the predominant wind direction from the northeast to the south, which remains largely consistent throughout the storm, even at the shorter 10 s intervals (Figure 4c). Wind speed increases at sunrise and mean wind speeds of about $10\,m\,s^{-1}$ are sustained throughout the storm, with maximum wind speeds between 10 and $20\,m\,s^{-1}$ (Figures 4d and 4e). ERA-Interim reanalysis data [*Dee et al.*, 2011] for October 2012 over all Antarctic sea ice suggest that 30% of near-surface wind speeds over sea ice were $> 10\,m\,s^{-1}$, and when precipitation > 2 cm/day was predicted, 58% of wind speeds were $> 10\,m\,s^{-1}$. Moreover, ERA-Interim 2 m air temperatures during predicted snowfall events during the same month most often fell within the range of temperatures observed during this event. Thus, we expect that the meteorological forcing during this blowing snow event to be common, and so similar events are likely widespread in spring, though the nature of the snow distribution may be expected to vary depending on particular meteorological and snow and ice morphological conditions. For instance, the volume of redistribution observed here may be large due to the relatively deep snowpack encountered during the experiment. Snow particle counts are highest at the lowest sensor, located within the saltation layer (Figures 4f and 4g). Wind speed thresholds of the order of $4\,m\,s^{-1}$ (at 2.36 m measurement height) for noticeable blowing snow at the lowest sensor were exceeded around sunset on 21 October and again around midnight of the same evening, after which the onset of the storm at sunrise causes continuous transport until the lowest sensor ceased recording around sunset on 22 October. Sensors higher on the mast continued to record falling and/or blowing snow for several hours (Figure 4f). It is anticipated that saltating snow continued to drift over the surface until the wind slackened (see Figures 4d and 4e).

3.2. Surface Topography

The sea ice/snow surface is composed of multidirectional and elongated snow dunes formed behind aerodynamic obstacles generally consisting of protruding ice or previously existing snow dunes. These features can be seen in Figures 2 and S1–S5 in which a series of detailed subsections of the pre-storm and post-storm surfaces are shown. The snow dune features prior to the storm show evidence for deposition during multiple events, including cross bedding from dunes at different angles (Figure S1). Two dominant orientations are evident, with broad dunes of up to ~30–60 m long oriented at 15–20° relative to the survey reference frame and thinner dunes up to about 20 m long oriented at about 30–45°. This is supported by semivariogram analysis [e.g., *Sturm et al.*, 1998], with peaks in the range of the variogram at ~10 and 20 m east-west (in the floe centric reference frame) and 40 m in the north-south. Both sets of dunes (particularly evident on the former) exhibit extensive scalloped erosional (sastrugi) features (Figures S2–S5). Many of the sastrugi features remain largely intact after the storm. While many of the snow features develop as drifts behind obstacles, many have sastrugi features, and some barchan dunes superposed on other snow features are apparent (e.g., Figure S2a, top left). These plots also suggest that erosion of existing dunes was slight (see also section 3.3 below) and the new dunes represent new deposition, rather than simply a reorientation of existing dunes.

Subsequent to the storm, marked changes are observed, principally as a consequence of newly accumulated dunes oriented along the direction of the wind (roughly parallel to the survey grid). Thus, the newer dunes are oriented at between 15° and 45° to the preexisting dunes. These new dunes (more prevalent on the left hand portion of the survey area; see Figures 1, 2, and S2) range from about 30 m to more than 100 m (seen extending beyond the survey in Figure 1). The longest deposition features appear to occur as dunes forming behind subsequent obstacles coalesce. New erosion patterns, on the other hand, are less evident and less
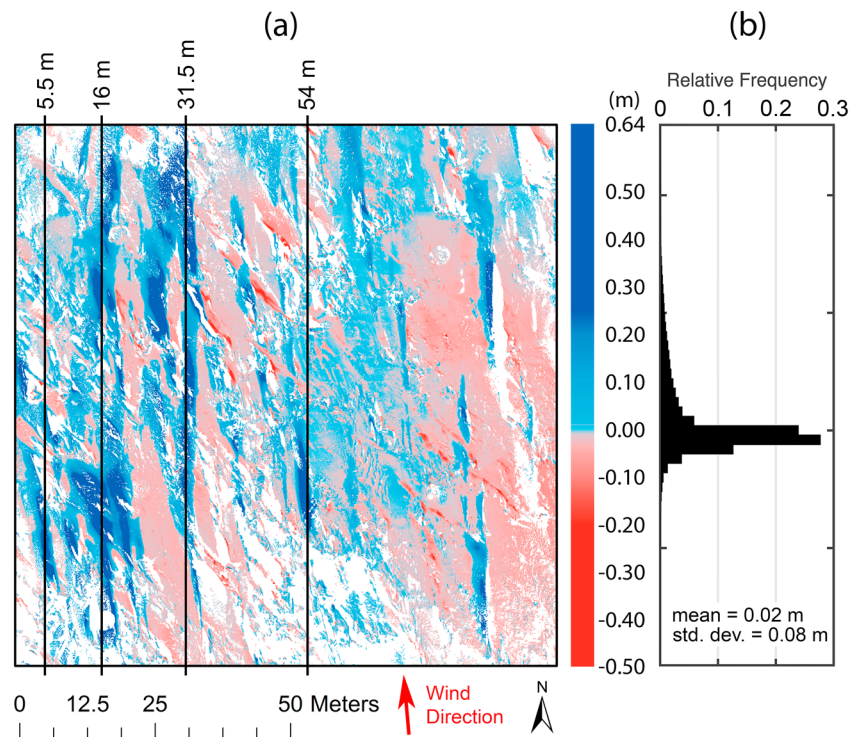
Figure 5. (a) Snow depth change between the pre-storm and post-storm surfaces at the 10 cm horizontal scale. The vertical black lines mark the location of the profiles in Figure 6. The predominant wind direction (175°) for the period with measured particle transport is indicated by the red arrow. No data areas are in white. (b) Empirical distribution function of snow depth change.

pronounced, although they cover a larger percentage of the surveyed area. The exception being the erosion of the preexisting dunes oriented at 30°–45°, which is more pronounced.

Comparison of the observed snow drift features with empirical relationships between manmade obstacles and snow drift lengths and volume [e.g., *Tabler*, 1980] is problematic, because of the observed cross bedding of the drifts, extension of drifts across multiple obstacles, highly variable morphology of the obstacles, and lack of a clear metric to use for obstacle size when mostly buried by existing snow structures. Note that although the dunes form behind such obstacles, they do not always do so (Figure 2b), so any relationship between obstacles and dune size and shape is unclear. Of note, however, is that these dunes are comparable in size to some drift features reported previously [*Radionov et al.*, 1997; *Sturm et al.*, 1998, 2002], although the longest dunes seen here are exceptional (perhaps as a result of the heavily deformed ice).

3.3. Elevation Differences

The patterns of elevation change, obtained as the difference between pre-storm and post-storm elevations at the 10 cm scale (Figure 5a), reflect patterns of erosion and deposition of snow due to the strong wind during the storm. Details of these changes are also highlighted in Figures 2c, 2d, and S2–S5. The mean elevation change is 2 ± 1 cm over the surveyed area (Figure 5b). This represents a relatively small mass gain despite large mass relocation. The mechanisms leading to the observed snow surface elevation differences before and after the storm can be described by two primary processes: erosion and deposition of snow, and ice deformation and ridging. For this floe, surface topography likely played a significant role in controlling the original deposition (pre-storm).

Figure 1 shows that the floe was composed of ice floes that had broken and frozen back together, with the ice ridges at the floe boundaries providing features behind which snow dunes could initiate. The association of dune structures with large ice rubble blocks (detail in Figure 2) suggests that ridges provide sites for accumulation of deeper snow and wind scoured features. This is consistent with previous observations of drift structures on both Arctic and Antarctic [*Radionov et al.*, 1997; *Sturm et al.*, 1998, 2002; *Massom et al.*, 2001].
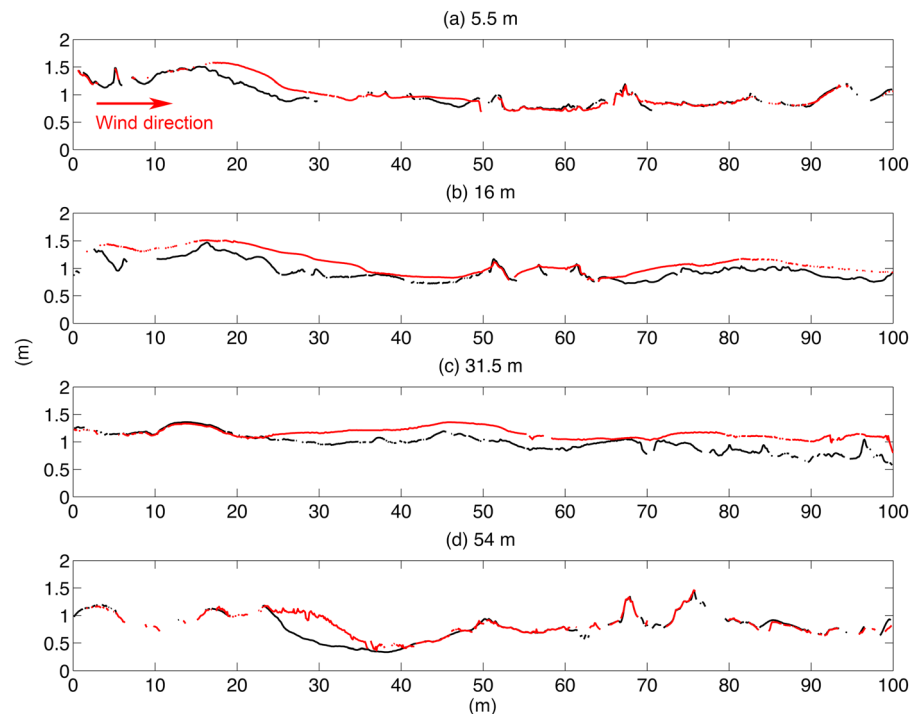
Figure 6. Sample surface profiles of the pre-storm (black) and post-storm (red) surfaces. Profile locations are indicated in Figure 5 by the vertical black lines. The *x* axis increases from south to north and the predominant wind direction during the storm is indicated by the red arrow.

Deposition occurred behind aerodynamic obstacles, consisting of protruding ice and previously existing snow dunes (Figure 5). These newly formed dunes extend for several tens of meters, even across the 100 m domain as can be seen on the left side of the domain (e.g., sample profiles in Figure 6). These sample profiles illustrate how snow deposition is enhanced behind aerodynamic obstacles according to their alignment to the predominant wind direction (indicated by the red arrows in Figures 5 and 6). Deposition occurs over 2690 m^2 (26.9% of the 100 m × 100 m area), while erosion occurs over 4320 m^2 (43.2% of the 100 m × 100 m area) (Figure 5a). Elevation differences over the remaining 29.9% (at this bin scale) of the 100 m × 100 m area are not available because there is a percentage of each individual surface left unsurveyed due to scan shade behind elevated pressure ridges and snow dunes. However, as mentioned in section 2, at the 1 m scale, only ~2% of the floe has no data. Assuming that on small scales the regions without data are not biased toward deposition or erosion, we can estimate the erosion and deposition over the entire floe by scaling by the area that contains data. This gives areas of erosion and deposition of 62% and 38%, respectively. At bin scales of 25 cm (15% no data) the areas are almost identical at 61% and 39%, and at 100 cm (2% no data) the areas are 58% and 42%. We infer that the larger differences at 100 cm are a result of the smaller-scale erosion and deposition features not being as well resolved. Other aggregate scale metrics (e.g., mean thicknesses) are not sensitive to the binning scale. This strongly suggests that on the aggregate, the data at 10 cm bin scale are a representative sample of the entire survey area. Thus, for the analysis that follows, we have scaled the results to provide estimates for the entire survey grid.

The local thickness changes of depositional features were significant relative to the mean snow depth of 52 cm; mean elevation changes of deposition features were 9.2 cm, with depositions of > 0.10 m covering an estimated 14% of the area. Depositions greater than 50 cm occurred over only 12 m^2 (~0.12% of the 100 m × 100 m area). Erosional thickness changes were significantly less, despite covering a greater area, with a mean loss of only 2.5 cm. Note that this mean loss was remarkably consistent across the survey area, varying between 2.2 and 2.9 cm when subsampling the area into four quarters. The great majority of the change (97% of the 100 m × 100 m area) has erosion or deposition thickness changes less than 25 cm. The deepest erosion changes are concentrated on the upwind side of previously existing snow dunes oriented at the steepest angle (~45°) with respect to the predominant wind direction during the storm (notice the deeper

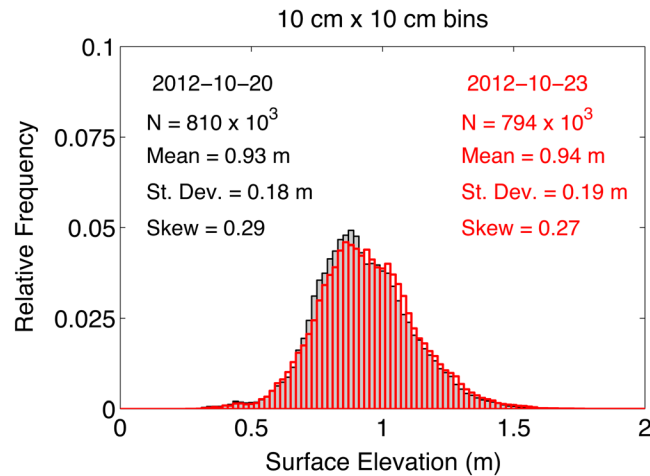**Figure 7.** Empirical distributions of surface elevation before and after the snowstorm for a 10 cm × 10 cm grid size. Coverage of each surface is represented by the number of 10 cm gridcells with data (*N*, with a maximum of 10^6 to cover the 100 m × 100 m area). Statistical moments of each of the distribution is also included.

red areas aligned diagonally in Figure 5a). The deepest accumulation changes are concentrated toward the center of the newly formed elongated dunes. Note that range errors between repeat scans as determined by collocated ridge peaks (where little to no snow would have been eroded or deposited) in both scans are negligible compared to the thickness of snow deposited or eroded adjacent to ridges or in level areas (Figure 6). This indicates that any potential TLS ranging error has little impact on the results and analysis presented here. However, the mean erosion (2.5 cm) is relatively small compared to the estimated error (~1 cm for the mean; 3 cm for an individual bin), so some caution is warranted in interpreting the small, but broad-scale, erosion patterns seen in Figure 5. The patterns of deeper erosion observed on the dune features at the steepest angles to the wind are more clear.

3.4. Surface Topography Statistics

Empirical probability distribution functions of surface elevations show little change between the pre-storm and post-storm surfaces (Figure 7). Statistical distributions are approximately Gaussian shaped although slightly positively skewed, with mean values of 93 and 94 cm, standard deviations of 18 and 19 cm, and skewness of 29 and 27 cm for the pre-storm and post-storm surfaces, respectively. Despite the marked changes in the surface patterns, the storm caused little change to the empirical distributions of elevation at the plot scale (e.g., 100 m × 100 m). This is likely due to the already deep snow cover prior to the storm, with pronounced dune structures (as seen in Figures 1 and 2). Nevertheless, this suggests that over large enough scales, the statistics of surface elevation may be reasonably stable in time for a given ice type. If confirmed by further observations, this may permit representation of complex and spatially variable properties of the ice cover by simple statistical models.

The two-dimensional correlation function of the pre-storm surface shows clear anisotropy with much longer spatial memory (i.e., slower correlation decay with distance) along the direction of the predominant snow dunes (Figure 8). Along this principal direction, correlation values decay to close to zero at lags of around 25 m. Perpendicular to this direction, correlations decay much more rapidly, reaching values close to zero at just under 10 m. These decorrelation scales are consistent with the observed scale of the dunes as described above. The spatial patterns of snow deposition highlighted in Figures 2a and 2b are reflected in the two-dimensional correlation function (Figure 8). The newly deposited post-storm dunes aligned with the vertical *y* axis cause only minor changes in the two-dimensional correlation function (Figure 8, red contours). The alignment of the new snow dunes, which display a rotation of about 15–45° clockwise with respect to the previously existing snow dunes, causes only a minor change of the principal direction of anisotropy, and the decay in the correlation is only slightly extended, as evidenced by the contours that lie very close to those of the pre-storm surface.

The log-log plots of the power spectral densities of the pre-storm and post-storm surfaces follow a power law relationship of the type $k^{-\beta}$ (where *k* is the frequency and *β* is the spectral exponent, seen as the slope of the relationship in the log-log space) for scales smaller than 10–20 m (Figure 9). Above these scales, the power spectra flatten out indicating a more uniform contribution of these lower frequencies (larger spatial scales) to the total variance and a loss of autocorrelation over these scales. Spectral slopes are reduced by a small degree after the storm, going from 2.58 and 2.36 to 2.44 and 2.27 in the *x* and *y* directions, respectively.
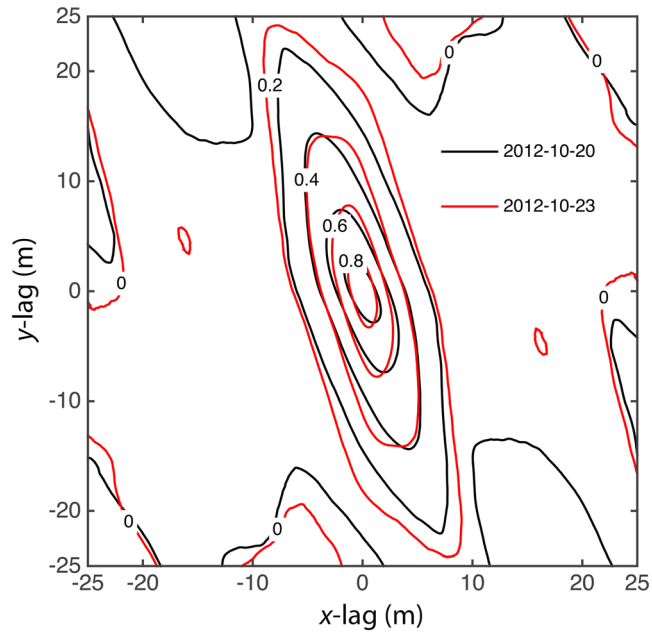
Figure 8. Two-dimensional correlation functions of the pre-storm and post-storm ice floe surfaces.

These changes indicate only a small change in the geometrical surface roughness after the snowstorm, although it should be noted that these changes reflect an average in each direction as the spectra of the profiles is averaged over the *x* and *y* directions. Whether or not these changes translate to a change in the integrated surface drag force exerted by the wind on the surface is a topic that the authors are exploring using large eddy simulations (LES) of the wind flow over the sea ice surfaces captured during SIPEX-2 [*Giometto et al.*, 2013; *Trujillo et al.*, 2014].

3.5. Snow Loading

While the mean elevation change of 2 ± 1 cm is relatively small, if we express these observations in terms of volumes and estimated mass changes, a more interesting picture emerges. The estimated integrated volume of erosion over the surveyed area is $158 \, \text{m}^3$ versus $352 \, \text{m}^3$ of deposition, which translates into $193 \, \text{m}^3$ of
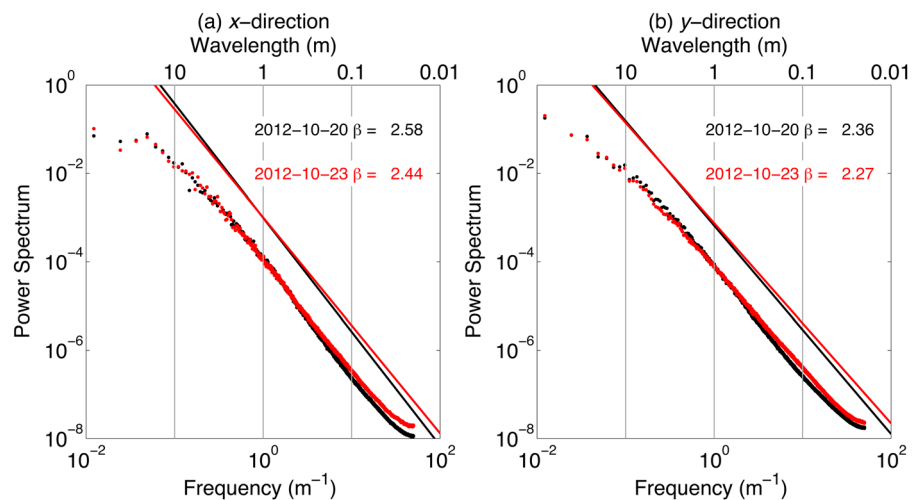

Figure 9. One-dimensional power pectral densities (point markers) along the *x* and *y* directions for the pre-storm and post-storm surface elevations. Results for the pre-storm and post-storm surfaces are shown in black and red, respectively. The solid lines indicate the power spectrum slope (β) for the higher frequencies (smaller spatial scales).
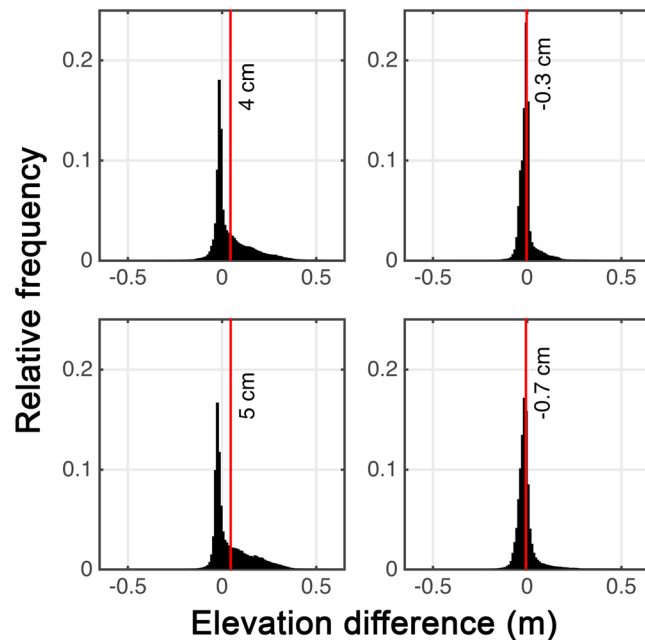
Figure 10. Histograms of elevation difference for four 50 m × 50 m subdivisions of the 100 m × 100 m area. The red vertical lines indicate the mean elevation difference. The four histograms are located in the figure such that the panels correspond to the location of the subarea within the 100 m × 100 m domain.

newly deposited snow, in itself higher that the total amount of eroded snow. This means that deposition volumes amount to more than twice the erosion volumes over the surveyed area. If we assume a mean snow density of this eroded and deposited snow of 300 kg m^{-3} (snow pit measurements on 23 October indicated a mean profile density of 295 kg m^{-3} and minimum and maximum densities of 191 kg m^{-3} and 373 kg m^{-3}, respectively), we have an estimated new water mass of 58 metric ton.. A 100 m drilling transect at this ice station along the left boundary of the 100 m × 100 m plot had an average ice thickness of 4.87 m [*Hutchings et al.*, 2015], with a mean snow depth in the survey area from snow probing of 0.52 m (for a total volume of 5200 m^3). This suggests the new mass load on the floe was low with respect to the ice mass and, hence, would not cause significant loading. However, over a thinner ice floe such an additional new mass could potentially lead to additional submersion, particularly under differential loading.

To analyze the differential loading caused by this particular storm, the distribution of snow erosion and deposition for subdivisions of the study area in four (50 m × 50 m; Figure 10) and sixteen (25 m × 25 m; Figure 11) subareas were obtained. This disaggregation shows that at smaller scales, changes in local differential loading as a result of new wind driven deposition and erosion are clearer, with the subareas toward the left side of the 100 m × 100 m plot receiving larger amounts of the newly deposited snow (e.g., compare the mean elevation difference toward the left side of the study area versus the decrease toward the right). This differential loading becomes clearer with higher levels of disaggregation, which can cause unbalanced loading of the floe, increasing the possibilities for partial flooding. On a thicker floe such as the one here, this differential loading would likely cause little imbalance since the new snow load is relatively low compared to the ice thickness; However, the effect may be more considerable over a thinner ice floe with lower relative ice mass with respect to that of the snowpack.

4. Discussion

Pre-storm measurements indicate strong correspondence in atmospheric conditions across the floe supported by independent measurements of temperature, wind direction, and speed at two masts separated by 228 m (Figure 3 and Table 2). This suggests that the atmospheric drivers of snow redistribution across the survey area were relatively uniform. However, the lower correlations (0.68–0.81 at 10 s and 0.78–0.90 at 1 min) between wind speeds at these two locations when compared to those of other atmospheric parameters also reflect the local effects of surface morphology on the wind flow in the lower boundary layer. Correlations between wind speeds at the two masts are strongest at the highest anemometers (Figure 3c and Table 2), highlighting the decreasing influence of the surface properties on the wind field with height above the surface. This can also be explained by the corresponding decrease in mean eddy size at lower elevations, which is a known feature of boundary layer dynamics close to the surface. Also, for each height, the scatter increases with wind speed as turbulence also increases. Pre-storm observations also highlight clear night-day transitions during these more calm conditions, with relatively low winds at sunrise and increasing slowly
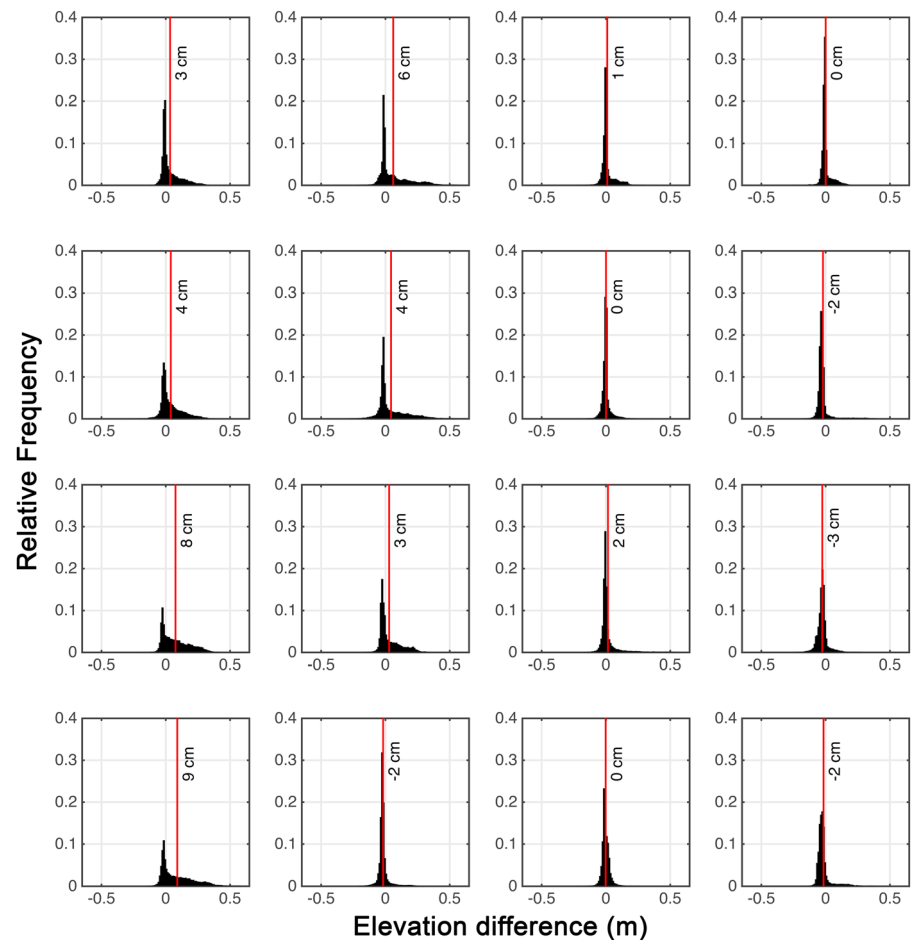
Figure 11. Same as Figure 10 but for 16 25 m × 25 m subdivisions of the 100 m × 100 m area. The red vertical lines indicate the mean elevation difference. The 16 histograms are located in the figure such that the panels correspond to the location of the subarea within the 100 m × 100 m domain.

following increases in incoming shortwave radiation. During the storm period, day-night-day transitions are less evident, with only slight increases in temperature differences during the day, contrary to what was observed during the pre-storm period. Also, the time series of temperature difference and directions are more stable during the storm period, with little fluctuation, contrary to what was observed prior to the storm (Figure 4). Snow particle counts highlight the characteristics of snow transport processes during this storm, with the great majority of particles being transported in the saltation layer just above the surface (Figures 4f and 4g). High winds are sustained throughout the storm for an extended period, with 10 s mean speeds greater than 10 m s^{-1} for 12 h at the upper sensor (2.36 m; Mast B) (3 h at the lower sensor at 0.57 m). The majority of the snow transport is observed during this period.

These results highlight some of the potential of repeat, fine-scale mapping of ice floe surfaces to examine event driven processes that have been difficult to capture on sea ice. During SIPEX-2, we successfully captured ice floe surface topography at scales ranging from centimeters to decimeters over an area of 100 m by 100 m. These results offer a level of detail that permits quantitative determination of geometric and statistical surface changes due to a precipitation and blowing snow event over broad areas. Data sets such as these will also be useful for a variety of applications, including the characterization of aerodynamic surface roughness and its relationship to surface wind profiles and high-resolution three-dimensional modeling of winds and blowing snow over sea ice. Repeat spatial mapping also provides the possibility of capturing changes in the sea ice surface roughness as a result of ice dynamics events. The present data set provides the necessary detail for high-resolution large eddy simulations (LES) and particle transport modeling. Such efforts, with more and broader-scale surveys have the potential to bridge gaps between point/local scales and small-scale processes, and larger model scales.

The small differences in the statistical properties of the surface topography before and after the storm raise an important question: are the differences in the surface morphology of sea ice, in particular, as a consequence of snow deposition and/or redistribution, important when characterizing surface interactions between atmospheric winds and surface features at larger scales? Our results show noticeable changes in the spatial patterns of snow distribution, including significant local thickness changes that do not translate into changes in the statistical distribution functions of elevation (Figure 7). Similarly, the two-dimensional correlation functions show only a minor rotation of the principal direction of anisotropy and slightly longer spatial memory (Figure 8), although these changes likely would have been more pronounced if the alignment of the new snow dunes (and predominant winds) were at a greater angle to that of the previously existing snow dunes. These results, in combination with small differences in the average surface roughness represented by the power spectrum exponents of the pre-storm and post-storm surfaces (Figure 9), suggest that the change in the surface as a consequence of snow redistribution does not represent major changes in the spatial statistics and surface structure at larger scales (e.g., $100 \, \text{m} \times 100 \, \text{m}$). Nevertheless, because the scales of the snow features are large relative to the survey area, we cannot be certain whether this behavior is representative on an aggregate scale; larger-scale surveys will be required to determine over what scales these statistics become invariant (and likely, they will depend on ice type and snow conditions).

It may also be the case that the statistics remained relatively unchanged because the new dunes were broadly aligned in the same general direction as existing dunes (at angles of 15–45°), and the development of new dunes occurred over only part of the survey area. If the winds were at a greater angle to the existing dunes, these may have provided more features for initiating new dunes and so permitting greater snow accumulation and creating the cross-hatched dune patterns that are commonly seen on sea ice floes or they may have promoted increased erosion of the existing dunes. Notably, greater erosion was observed on the upwind crests of dunes aligned at a greater angle to the wind (~30–45°), while less pronounced and more uniform erosion occurred on the more prevalent, broader dunes oriented at 15–20°.

For less deformed floes with fewer obstacles, we might expect the long dune structures formed in the lee of these obstacles to be fewer and thus contribute less to the surface roughness statistics. For example, at SHEBA, large drifts around ridges covered a relatively small portion of the surface area of the ice [*Sturm et al.*, 2002]. On level sea ice, barchan dunes have been observed to be the dominant snow surface feature [*Massom et al.*, 2001; *Petrich et al.*, 2012]. The surface statistics might also change under different deposition conditions, for instance, significant snow accumulation in light wind conditions that might be expected in late spring or early summer.

The elevation differences provide insight into the process of snow redistribution by wind over Antarctic sea ice. Over the study area, erosion occurred over a larger area (62% of the $100 \, \text{m} \times 100 \, \text{m}$ area), although erosion depths were low when compared to deposition, which occurs over 38% of the $100 \, \text{m} \times 100 \, \text{m}$ area (Figure 5). On average, surface elevation increases only by $2 \pm 1 \, \text{cm}$, which is equivalent to an estimated total volume increase of $193 \, \text{m}^3$ over the surveyed area. Although this 2 cm increase may appear small, local thickness changes were significant relative to the snow depth, and the volume of added snow over the area is larger than the eroded mass itself. Thus, these patterns of change may be important for ice mass balance on the subfloe scale. The patterns of erosion and deposition are partially explained by the predominant wind during the storm (Figure 4) and the alignment of surface features.

These estimates raise additional questions regarding the origin of the newly deposited snow. Two alternative sources are precipitation or from an upwind erosional source. The information available does not allow for accurate discrimination between these two sources. Likewise, it is not possible with these observations to determine how much of the precipitated snow during the storm was deposited on the floe or transported elsewhere (e.g., to be deposited in potentially rougher ice elsewhere or in leads).

The best available estimates of precipitation are from atmospheric reanalysis products, though their reliability for quantification of individual precipitation events over Antarctic sea ice is highly uncertain. Era-Interim reanalysis appears to provide the best representation of cyclones in the Southern Ocean [*Naud et al.*, 2014] and likely the most reliable estimates of precipitation over Antarctic sea ice [e.g., *Bromwich et al.*, 2011]. The spatial pattern of reanalysis precipitation and cloud liquid water path from NASA's

Moderate Resolution Imaging Spectroradiometer also shows good agreement during the storm, and snowfall estimates during the study period were consistent with observations of snowfall events from the ship (not shown). However, as our observations were taken near the edge of the observed storm and because of the completely unknown accuracy of precipitation from individual storms over the Southern Ocean, any quantitative comparison should be made with caution. Nevertheless, the reanalysis estimates that 3.7 cm of snow (assuming a density of $300\,kg\,m^{-3}$) fell during the storm. This suggests that perhaps half of the snowfall may have been transported and deposited elsewhere, consistent with the observations of *Leonard and Maksym* [2011], although it may well have been less.

Given the small survey area, one question is how representative local conditions were of snow redistribution more broadly. This would require that the $100\,m \times 100\,m$ area is representative of the larger ice floe and that this scale exceeds a threshold scale over which the processes of snow erosion and deposition become statistically uniform. This is likely true for erosion but is less clear for deposition, given the scale and distribution of the new depositional features. Qualitative comparison of post-storm aerial imagery of snow dune structures inside and outside of the survey area (see Figure 1; also seen in imagery with greater areal coverage—not shown) show similar sizes and orientation of dunes, and ridge frequency and size. This suggests that the deposition and erosion patterns may be representative of snow redistribution processes across the floe, and not due to anomalous features or behavior within the survey grid, although we cannot determine if the depositional and erosional thicknesses are similar elsewhere. Moreover, the scale of the new dunes is large enough that the $100 \times 100\,m$ grid may be of insufficient size to capture all scales of variability across this particular floe.

Although these observations are of only a single storm, we can infer certain potential processes of importance that have important implications for snow redistribution more broadly by placing these observations in context. We note that snow erosion occurred over 62% of the area. Shipboard observations of precipitation frequency show that there had been no accumulation since 19 October, 3 days prior to the storm, and perhaps little for 10 days prior. This shows that despite warm conditions (i.e., ~ -10 to $-5\,°C$, as observed during daylight hours in the area in the days before the storm) that might promote sintering and immobilization of snow grains, aeolian transport of older snow occurred during the event, although losses were small over the survey area except for dunes oriented at a relatively steep angle to the wind direction (Figure 5). Both shipboard observations and reanalysis estimates indicate approximately seven distinct precipitation events during the month. Given the high frequency of cyclones in the region [*Simmonds and Keay*, 2000], this suggests that snow redistribution in autumn may be frequent and widespread, despite relatively warm temperatures, and must be considered when estimating snow mass balance on sea ice.

Comparison of meteorological conditions observed during the storm with ERA-interim reanalysis also suggest that this storm may have been typical. For reanalysis precipitation events (>2 cm snowfall per day or 6 mm water equivalent) forecasted over sea in October 2012, daily mean temperatures were almost always between $-10°C$ and $0°C$—relatively warm but comparable to those observed during the storm described herein. Daily mean 10 m wind speeds during these events were also typically $10-15\,m\,s^{-1}$, which also compares well with wind speeds observed during this storm (see Figure 4). We also note that the thick, heavily deformed ice and deep snow observed on the floe may be typical of spring ice near the coast [*Kwok and Maksym*, 2014; *Williams et al.*, 2015]. Thus, it is reasonable to infer that the conditions (both surface and meteorological) are fairly common for a snowstorm event on Antarctic sea ice in late spring.

5. Conclusions and Outlook

The detailed survey of the snow on a sea ice surface conducted in this study has allowed the detection of several new observations which have not been discussed thus far in the literature. One first technical result is that snow surface changes that occur at time scales of hours can be quantified with accuracy in the 0.01–0.03 m range. The accurate relative positioning of the surfaces allowed quantification of the surface mass balance through the determination of erosion and accumulation patterns and depths for the first time. The results show that the snowstorm resulted in net erosion over approximately 62% of the $100\,m \times 100\,m$ area and net deposition over approximately 38% of the $100\,m \times 100\,m$ area. This particular storm, which lasted about 20 h, deposited more than twice as much snow as it eroded over the surveyed area. While the average

amount of erosion was small (mean of 2.5 cm), it was evenly distributed over the area of net erosion, with the exception of deeper erosion of the preexisting dune crests that were oriented most steeply to the direction of the wind. The deposition (mean of 9.2 cm) was unevenly distributed—predominantly in the large new drifts. Likewise, while the average change in snow depth was quite small (2 ± 1 cm) compared to the mean snow depth (52 cm), there were relatively large local changes in snow depth. This is an important consideration in evaluating the representativeness of point measurements for evaluating snow and ice mass balance (e.g., from autonomous ice mass balance buoys).

It is not possible to conclusively determine the source of this new deposition nor whether these observations are representative of a broader area. However, our best estimate of the total precipitation (from atmospheric reanalysis) indicates that precipitation (~3.7 cm) exceeded the mean deposition. This suggests that the new mass likely originates from precipitation and that a significant fraction of the new snowfall may have been redistributed to other areas of the floe or lost to leads.

This investigation is a proof of concept of how spatial snow deposition rates from precipitation and wind redistribution processes over sea ice can be determined, which is currently an unresolved problem. Airborne lidar [e.g., *Kurtz et al.*, 2013], and drone-based photogrammetric methods [e.g., *Nolan et al.*, 2015] can provide the additional spatial coverage required for broader-scale aggregate estimates. Achieving the centimeter-scale vertical accuracies necessary to detect the small changes induced by precipitation and blowing snow processes we show here are a challenge for airborne platforms. However, some studies have shown that with good ground control vertical errors as low as 4 cm are possible [*Harwin and Lucieer*, 2012]. This capability should allow studies over larger areas to show how well these snow deposition rates can indeed be used to constrain precipitation.

Statistical properties of the snow surface remained stable after the storm despite the modification of the original deposition patterns and the new elongated dunes following the principal wind direction. This may have been a particular result for this case study, but if this behavior can be confirmed for other ice floes and storm events, this has implications for larger-scale models, which need such spatial statistics to characterize surface elevations, snow distribution, and aerodynamic roughness to correctly represent subgrid heterogeneity of physical properties and sea ice processes. If the finding is indeed more general (for example, for ice floes of a particular type and age and thus similar snow surface and snow depth properties), then parameterization of the equilibrium surface properties (in a statistical sense) for different sea ice and snow classes may be possible. Alternatively, if sufficient similar observations can be made, it may be possible to develop time-dependent parameterizations of these processes.

It is important to note that the snow and ice conditions at this station were unusual, with ice thicker and more deformed than is commonly found elsewhere, and with deeper snow accumulations (mean depths of 52 cm) than the 10–30 cm typical in the outer pack in spring [*Massom et al.*, 2001]. We expect surface snow distribution statistics to change significantly as snow first accumulates and dune features first develop on young sea ice. This might evolve to behavior similar to that observed here once significant accumulation has developed and where long dune structures can develop on older ice with ridge and rubble surface elements to initiate dune formation. One possible scenario is that once significant accumulation has developed on rough sea ice, a state of stability may be reached, with a mature snow cover that can be characterized by little change in surface topography statistics. Thus, in this case, the role of surface morphology in controlling erosion and deposition during drifting and blowing snow events may be to maintain this "steady state", whereby the alignment of the predominant dune features may change, but their statistical properties show modest change. This has some similarities to prior observations where snow structure characteristics on Arctic sea ice were similar even for different ice classes [e.g., *Sturm et al.*, 2002]. However, the statistics may remain relatively unchanged because the new dunes were aligned in broadly the same direction as existing dunes, or that the initial snow and ice conditions were conducive to the observed deposition patterns. For example, for ice with fewer surface features, or for significant accumulation under light wind conditions, we might expect the surface roughness statistics to change significantly.

Despite these limitations, this study provides a template for resolving how these different scenarios may affect snow and sea ice mass balance at larger scales. This will require similarly detailed experiments over broader and more varied sea ice environments so that improved aggregate scale parameterizations of how snow deposition, erosion, and roughness evolve on a range of ice types can be made.

References

Ackley, S. F., and C. W. Sullivan (1994), Physical controls on the development and characteristics of Antarctic sea-ice biological communities—A review and synthesis, *Deep Sea Res., Part I*, 41(10), 1583–1604.

Andreas, E. L., and K. J. Claffey (1995), Air-ice drag coefficients in the Western Weddell Sea: 1. Values deduced from profile measurements, *J. Geophys. Res.*, 100, 4821–4831, doi:10.1029/94JC02015.

Bagnold, R. A. (1941), *The Physics of Wind Blown Sand and Desert Dunes*, pp. 265, Methuen Ltd., London.

Bromwich, D. H., F. M. Robasky, R. I. Cullather, and M. L. Vanwoert (1995), Atmospheric hydrologic-cycle over the Southern-Ocean and Antarctica from operational numerical-analyses, *Mon. Weather Rev.*, 123(12), 3518–3538, doi:10.1175/1520-0493(1995)123<3518:Tahcot>2.0.Co;2.

Bromwich, D. H., J. P. Nicolas, and A. J. Monaghan (2011), An assessment of precipitation changes over Antarctica and the Southern Ocean since 1989 in contemporary global reanalyses, *J. Clim.*, 24(16), 4189–4209.

Clifton, A., J. D. Ruedi, and M. Lehning (2006), Snow saltation threshold measurements in a drifting-snow wind tunnel, *J. Glaciol.*, 52(179), 585–596, doi:10.3189/172756506781828430.

Cornish, V. (1914), *Waves of Sand and Snow and the Eddies Which Make Them*, Fisher Unwin, London.

Dee, D. P., et al. (2011), The ERA-Interim reanalysis: Configuration and performance of the data assimilation system, *Q. J. R. Meteorol. Soc.*, 137, 553–597.

Dery, S. J., and L. B. Tremblay (2004), Modeling the effects of wind redistribution on the snow mass budget of polar sea ice, *J. Phys. Oceanogr.*, 34(1), 258–271, doi:10.1175/1520-0485(2004)034<0258:Mteowr>2.0.Co;2.

Eicken, H., M. A. Lange, H. W. Hubberten, and P. Wadhams (1994), Characteristics and distribution patterns of snow and meteoric ice in the Weddell Sea and their contribution to the mass-balance of sea-ice, *Ann. Geophys.*, 12(1), 80–93, doi:10.1007/S00585-994-0080-X.

Eicken, H., H. Fischer, and P. Lemke (1995), Effects of the snow cover on Antarctic sea ice and potential modulation of its response to climate change, *Ann. Glaciol.*, 21, 369–376.

Filhol, S., and M. Sturm (2015), Snow bedforms: A review, new data, and a formation model, *J. Geophys. Res. Earth Surf.*, 120, 1645–1669, doi:10.1002/2015JF003529.

Fritsen, C. H., V. I. Lytle, S. F. Ackley, and C. W. Sullivan (1994), Autumn BLOOM of Antarctic pack-ice algae, *Science*, 266(5186), 782–784, doi:10.1126/Science.266.5186.782.

Giometto, M. G., E. Trujillo, K. C. Leonard, T. L. Maksym, C. V. Meneveau, M. Lehning, and M. B. Parlange (2013), LES modeling of wind over Antarctic snow-ice formations using a dynamic surface roughness approach, Abstract A43A-0223 presented at Fall Meeting, AGU.

Grünewald, T., M. Schirmer, R. Mott, and M. Lehning (2010), Spatial and temporal variability of snow depth and ablation rates in a small mountain catchment, *Cryosphere*, 4(2), 215–225, doi:10.5194/tc-4-215-2010.

Guest, P. S., and K. L. Davidson (1991), The aerodynamic roughness of different types of sea ice, *J. Geophys. Res.*, 96, 4709–4721, doi:10.1029/90JC02261.

Haas, C., D. N. Thomas, and J. Bareiss (2001), Surface properties and processes of perennial Antarctic sea ice in summer, *J. Glaciol.*, 47(159), 613–615, doi:10.3189/172756501781831864.

Harwin, S., and A. Lucieer (2012), Assessing the accuracy of georeferenced point clouds produced via multi-view stereopsis from Unmanned Aerial Vehicle (UAV) imagery, *Remote Sens.*, 4(6), 1573–1599, doi:10.3390/rs4061573.

Hutchings, J. K., P. Heil, O. Lecomte, R. Stevens, A. Steer, and J. L. Lieser (2015), Comparing methods of measuring sea-ice density in the East Antarctic, *Ann. Glaciol.*, 56(69), 77–82, doi:10.3189/2015AoG69A814.

Jeffries, M. O., S. Li, R. A. Jaña, H. R. Krouse, and B. Hurst-Cushing (1998), Late winter first-year ice floe thickness variability, seawater flooding and snow ice formation in the Amundsen and Ross Seas, in *Antarctic Sea Ice: Physical Processes, Interactions and Variability*, *Antarct. Res. Ser.*, vol. 74, edited by M. O. Jeffries, pp. 69–88, AGU, Washington, D. C.

Kurtz, N. T., and T. Markus (2012), Satellite observations of Antarctic sea ice thickness and volume, *J. Geophys. Res.*, 117, C08025, doi:10.1029/2012JC008141.

Kurtz, N., S. L. Farrell, N. Galin, J. P. Harbeck, R. Lindsay, V. D. Onana, B. Panzer, and J. G. Sonntag (2013), Sea ice thickness, freeboard, and snow depth products from Operation IceBridge airborne data, *Cryosphere*, 7, 1035–1056, doi:10.5194/tc-7-1035-2013.

Kwok, R., and T. Maksym (2014), Snow depth of the Weddell and Bellingshausen sea ice covers from IceBridge surveys in 2010 and 2011: An examination, *J. Geophys. Res. Oceans*, 119, 4141–4167, doi:10.1002/2014JC009943.

Kwok, R., G. F. Cunningham, H. J. Zwally, and D. Yi (2006), ICESat over Arctic sea ice: Interpretation of altimetric and reflectivity profiles, *J. Geophys. Res.*, 111, C06006, doi:10.1029/2005JC003175.

Ledley, T. S. (1993), Variations in snow on sea-ice—A mechanism for producing climate variations, *J. Geophys. Res.*, 98, 10,401–10,410, doi:10.1029/93JD00316.

Leonard, K. C. (2009), Antarctic snow drift processes, PhD thesis, Columbia Univ., Columbia.

Leonard, K. C., and T. Maksym (2011), The importance of wind-blown snow redistribution to snow accumulation on Bellingshausen Sea ice, *Ann. Glaciol.*, 52(57), 271–278, doi:10.3189/172756411795931651.

Leonard, K. C., L. B. Tremblay, J. E. Thom, and D. R. MacAyeal (2011), Drifting snow threshold measurements near McMurdo station, Antarctica: A sensor comparison study, *Cold Reg. Sci. Technol.*, 70, 71–80.

Lewis, M. J., J. L. Tison, B. Weissling, B. Delille, S. F. Ackley, F. Brabant, and H. Xie (2011), Sea ice and snow cover characteristics during the winter-spring transition in the Bellingshausen Sea: An overview of SIMBA 2007, *Deep Sea Res., Part II*, 58(9–10), 1019–1038, doi:10.1016/j.dsr2.2010.10.027.

Li, L., and J. W. Pomeroy (1997), Estimates of threshold wind speeds for snow transport using meteorological data, *J. Appl. Meteorol.*, 36, 205–213, doi:10.1175/1520-0450(1997)036%3C0205:EOTWSF%3E2.0.CO;2.

Livingstone, I., G. F. Wiggs, and C. M. Weaver (2007), Geomorphology of desert sand dunes: A review of recent progress, *Earth Sci. Rev.*, 80(3), 239–257, doi:10.1016/j.earscirev.2006.09.004.

Maksym, T., and T. Markus (2008), Antarctic sea ice thickness and snow-to-ice conversion from atmospheric reanalysis and passive microwave snow depth, *J. Geophys. Res.*, 113, C02S12, doi:10.1029/2006JC004085.

Massom, R. A., et al. (2001), Snow on Antarctic Sea ice, *Rev. Geophys.*, 39, 413–445, doi:10.1029/2000RG000085.

Maykut, G. A., and N. Untersteiner (1971), Some results from a time-dependent thermodynamic model of sea ice, *J. Geophys. Res.*, 76(6), 1550–1575, doi:10.1029/JC076i006p01550.

Meiners, K. M., K. M. Golden, P. Heil, J. L. Lieser, R. Massom, B. Meyer, and G. D. Williams (2016), Introduction: SIPEX-2: A study of sea-ice physical, biogeochemical and ecosystem processes off East Antarctica during spring 2012, *Deep Sea Res., Part II*, 131, 1–6, doi:10.1016/j.dsr2.2016.06.010.

Naud, C. M., J. F. Booth, and A. D. Del Genio (2014), Evaluation of ERA-Interim and MERRA cloudiness in the Southern Ocean, *J. Clim.*, *27*(5), 2109–2124.

Nolan, M., C. Larsen, and M. Sturm (2015), Mapping snow depth from manned aircraft on landscape scales at centimeter resolution using structure-from-motion photogrammetry, *Cryosphere*, *9*, 1445–1463, doi:10.5194/tc-9-1445-2015.

Ozsoy-Cicek, B., S. Ackley, H. J. Xie, D. H. Yi, and J. Zwally (2013), Sea ice thickness retrieval algorithms based on in situ surface elevation and thickness values for application to altimetry, *J. Geophys. Res. Oceans*, *118*, 3807–3822, doi:10.1002/jgrc.20252.

Perovich, D. K., C. S. Roesler, and W. S. Pegau (1998), Variability in Arctic sea ice optical properties, *J. Geophys. Res.*, *103*, 1193–1208, doi:10.1029/97JC01614.

Perovich, D. K., T. C. Grenfell, B. Light, and P. V. Hobbs (2002), Seasonal evolution of the albedo of multiyear Arctic sea ice, *J. Geophys. Res.*, *107*(C10), 8044, doi:10.1029/2000JC000438.

Petrich, C., H. Eicken, C. M. Polashenski, M. Sturm, J. P. Harbeck, D. K. Perovich, and D. C. Finnegan (2012), Snow dunes: A controlling factor of melt pond distribution on Arctic sea ice, *J. Geophys. Res.*, *117*, C09029, doi:10.1029/2012JC008192.

Polashenski, C., D. Perovich, and Z. Courville (2012), The mechanisms of sea ice melt pond formation and evolution, *J. Geophys. Res.*, *117*, C01001, doi:10.1029/2011JC007231.

Powell, D. C., T. Markus, and A. Stossel (2005), Effects of snow depth forcing on Southern Ocean sea ice simulations, *J. Geophys. Res.*, *110*, C06001, doi:10.1029/2003JC002212.

Prokop, A. (2008), Assessing the applicability of terrestrial laser scanning for spatial snow depth measurements, *Cold Reg. Sci. Technol.*, *54*(3), 155–163, doi:10.1016/j.coldregions.2008.07.002.

Prokop, A., M. Schirmer, M. Rub, M. Lehning, and M. Stocker (2008), A comparison of measurement methods: Terrestrial laser scanning, tachymetry and snow probing for the determination of the spatial snow-depth distribution on slopes, *Ann Glaciol. Ser.*, *49*, 210–216.

Radionov, V. F., N. N. Bryazgin, and E. I. Alexandrov (1997), The snow cover of the Arctic Basin, Tech. Rep. APL-UW-TR 9701, 95 pp., Appl. Phys. Lab., Univ. of Washington, Seattle, Washington.

Raymond, B., K. Meiners, C. W. Fowler, B. Pasquer, G. D. Williams, and S. Nicol (2009), Cumulative solar irradiance and potential large-scale sea ice algae distribution off East Antarctica (30°E–150°E), *Polar Biol.*, *32*(3), 443–452, doi:10.1007/s00300-008-0538-5.

Schirmer, M., V. Wirz, A. Clifton, and M. Lehning (2011), Persistence in intra-annual snow depth distribution: 1. Measurements and topographic control, *Water Resour. Res.*, *47*, W09516, doi:10.1029/2010WR009426.

Simmonds, I., and K. Keay (2000), Mean Southern Hemisphere extratropical cyclone behavior in the 40-year NCEP-NCAR reanalysis, *J. Clim.*, *13*(5), 873–885.

Soohoo, J. B., A. C. Palmisano, S. T. Kottmeier, M. P. Lizotte, S. L. Soohoo, and C. W. Sullivan (1987), Spectral light-absorption and quantum yield of photosynthesis in sea ice microalgae and a bloom of Phaeocystis-Pouchetii from Mcmurdo Sound, Antarctica, *Mar. Ecol. Prog. Ser.*, *39*(2), 175–189, doi:10.3354/Meps039175.

Sturm, M., and R. Massom (2009), Snow and sea ice, in *Sea Ice*, edited by D. N. Thomas and G. S. Dieckmann, pp. 153–204, John Wiley & Sons, Oxford, U. K.

Sturm, M., K. Morris, and R. Massom (1998), The winter snow cover of the West Antarctic pack ice: Its spatial and temporal variability, in *Antarctic Sea Ice: Physical Processes, Interactions and Variability*, *Antarct. Res. Ser.*, vol. 74, edited by M. O. Jeffries, pp. 1–18, AGU, Washington, D. C.

Sturm, M., J. Holmgren, and D. Perovich (2002), The winter snow cover on the sea ice of the Arctic Ocean at SHEBA: Temporal evolution and spatial variability, *J. Geophys. Res.*, *107*(C10), 8047, doi:10.1029/2000JC000400.

Tabler, R. D. (1980), Geometry and density of drifts formed by snow fences, *J. Glaciol.*, *26*, 405–419.

Tin, T., and M. O. Jeffries (2001), Sea-ice thickness and roughness in the Ross Sea, Antarctica, *Ann. Glaciol.*, *33*(1), 187–193.

Toyota, T., R. Massom, O. Lecomte, D. Nomura, P. Heil, T. Tamura, D. Alexander, and A. Fraser (2016), On the extraordinary snow on the sea ice off East Antarctica in late winter, 2012, *Deep Sea Res., Part II*, *131*, 53–67, doi:10.1016/j.dsr2.2016.02.003i.

Trujillo, E., J. A. Ramirez, and K. J. Elder (2007), Topographic, meteorologic, and canopy controls on the scaling characteristics of the spatial distribution of snow depth fields, *Water Resour. Res.*, *43*, W07409, doi:10.1029/2006WR005317.

Trujillo, E., J. A. Ramírez, and K. J. Elder (2009), Scaling properties and spatial organization of snow depth fields in sub-alpine forest and alpine tundra, *Hydrol. Process.*, *23*, 1575–1590, doi:10.1002/hyp.7270.

Trujillo, E., M. G. Giometto, K. C. Leonard, T. L. Maksym, C. V. Meneveau, M. B. Parlange, and M. Lehning (2014), Spatially-resolved mean flow and turbulence help explain observed erosion and deposition patterns of snow over Antarctic sea ice, Abstract C22A-04, presented at Fall Meeting, AGU.

Trujillo, E., T. Maksym, R. Hoesli, M. Lehning and K. Leonard (2016), High resolution sea ice surface topography from the SIPEX-2 expedition, East Antarctica, 2012, École Polytechnique Fédérale de Lausanne; doi:10.16904/9.

Williams, G., T. Maksym, J. Wilkinson, C. Kunz, C. Murphy, P. Kimball, and H. Singh (2015), Thick and deformed Antarctic sea ice mapped with autonomous underwater vehicles, *Nat. Geosci.*, *8*, 61–67, doi:10.1038/ngeo2299.

Worby, A. P., M. O. Jeffries, W. F. Weeks, K. Morris, and R. Jaña (1996), The thickness distribution of sea ice and snow cover during late winter in the Bellingshausen and Amundsen Seas, Antarctica, *J. Geophys. Res.*, *101*, 28,441–28,455, doi:10.1029/96JC02737.